Respiratory Movement Correction in Emission Tomography

Mauricio Reyes Aguirre, Grégoire Malandain, Jacques Darcourt

INRIA

INSTITUT NATIONAL DE RECHERCHE EN INFORMATIQUE ET EN AUTOMATIQUE

Respiratory Movement Correction in Emission Tomography

Mauricio Reyes Aguirre — Grégoire Malandain — Jacques Darcourt

N° 5279

July 2004

Thème BIO

ISSN 0249-6399 ISRN INRIA/RR--5279--FR+ENG

INRIA
SOPHIA ANTIPOLIS

Respiratory Movement Correction in Emission Tomography

Mauricio Reyes Aguirre , Grégoire Malandain , Jacques Darcourt

Thème BIO — Systèmes biologiques
Projet Epidaure

Rapport de recherche n° 5279 — July 2004 — 47 pages

Abstract: In emission tomography, the process of image reconstruction has evolved since the utilization of the filtered back projection algorithm (FBP). Nowadays, iterative techniques incorporating statistical knowledge of the photon emission process has produced much interest among researchers, not only for the improvements achieved in image quality, but also by the possibility of incorporate corrections factors, like scattering, attenuation, etc.
One of the problems that has not been discussed in depth is the incorporation of correction methodologies due to patient breathing, which produces blur regions in lungs and cardiac images. Solutions like respiratory gating, that synchronize the breathing cycle of the patient and the data acquisition process, or correlated dynamic PET techniques that use external radioactive markers and list mode data, have been tested with improvements over the spatial activity distribution in lungs lesions, but with the disadvantages of requiring extra hardware or more expensive scanner systems. The objective of this study was to incorporate breathing-movement corrections directly to the phase of image reconstruction, without any additional acquisition protocol consideration. For this, a procedure of correction inside the probability matrix in the classical MLEM algorithm has been implemented which takes into account the spatio-temporal relationship of each voxel in the structure under study. We present 2D and 3D results from synthetic and realistic simulations showing the potential benefits of using this approach.

Unité de recherche INRIA Sophia Antipolis
2004, route des Lucioles, BP 93, 06902 Sophia Antipolis Cedex (France)
Téléphone : +33 4 92 38 77 77 —Télécopie : +33 4 92 38 77 65

Key-words: image reconstruction, respiratory movement, MLEM, nuclear medicine, emission tomography.

Correction du mouvement respiratoire en tomographie d'émission

Résumé : En tomographie d'émission, les procédés de reconstruction ont évolué des méthodes analytiques de rétro-projection filtrée, aussi utilisées en tomographie de transmission, à des techniques itératives qui incorporent une modélisation statistique de l'émission des photons par un élément radioactif. Ces dernières ont suscité un grand intérêt dans la communauté, non seulement par leur aptitude à améliorer la qualité des images reconstruites, mais aussi par leur capacité à incorporer divers facteurs de correction, prenant en compte la dispersion, l'atténuation, etc.

Toutefois, la prise en compte des mouvements du patient, en particulier des mouvements physiologiques (respiration, battement cardiaque), qui introduisent un flou dès l'acquisition des projections, flou que l'on retrouve lors de la reconstruction, n'a été abordé que superficiellement.

Jusqu'à présent, les techniques employées visent à adapter l'acquisition des données pour rendre la reconstruction d'un objet statique possible. Il s'agit par exemple de synchroniser l'acquisition des données avec le mouvement (comme la respiration), ou d'acquérir les détections en mode liste et d'utiliser alors une technique de corrélation dynamique qui nécessite l'ajout de marqueurs radioactifs externes supposés rendre compte du mouvement.

Dans le cadre de l'imagerie des poumons, ces techniques ont montré une amélioration de la quantification des lésions détectées, mais malheureusement au prix d'un protocole d'acquisition plus lourd (nécessitant des matériels supplémentaires et/ou plus coûteux), qui les rendent inapplicables a posteriori à la plupart des acquisitions en routine clinique.

L'objectif de ce travail est d'incorporer directement les corrections liés au mouvement dans le processus de reconstruction, sans avoir à agir en amont sur le processus d'acquisition. Pour ce faire, la technique proposée s'appuie sur un algorithme MLEM (*Maximum Likelihood Expectation Maximization*) dans lequel la matrice des probabilités prend en compte la contribution spatio-temporelle à chaque projection du voxel à reconstruire.

Nous présentons des résultats 2-D et 3-D, avec des expériences synthétiques et des simulations réalistes, qui montrent le bénéfice potentiel d'une telle approche.

Mots-clés : reconstruction d'image, mouvement respiratoire, tomographie d'émission

Contents

1 Introduction

Nowadays, several medical imaging modalities exist that allow the physicians to get an image-based description of an organ. This description can be either information of the anatomical structures under study or information of their functional behavior. This functional information has brought interest among physicians, physiologists, biologists, etc. due mainly to the richness of the information in the sense of detection and treatment of diseases like cancer in which the biochemical changes precede the anatomical ones, allowing earlier diagnosis and treatment. Furthermore, the combination of functional and anatomical modalities has also allowed improvements in diagnosis and following of diseases. All this, in addition with advances in data acquisition (i.e., higher resolutions, lower acquisition times, etc.), has caused a demand of better algorithms, like registration techniques to fusion modalities [40, 30, 29, 28, 47, 48, 7, 46, 14, 8, 9, 25], or image reconstruction algorithms that take a set of indirect measurement data and generate a visual representation of a variable of interest. For the latter, the widespread improvements in the techniques include better image resolutions, inclusion of physical corrections, faster reconstruction algorithms, etc. [18, 26, 1, 43, 36, 27]
Unlikely to CT, MRI and others techniques that use an external source of radiation to visualize the different structures (measuring absorption coefficients (CT), protons density (MRI), etc.), in emission tomography (EM) an internal source of radiation (commonly injected) is used, called radio-isotope. The type of radio-isotope makes a difference between EM techniques, being PET (Positron Emission Tomography) and SPECT (Single Photon Emitting Computed Tomography) the classical ones. The radio-isotope goes "attached" to a tracer which is selected depending on the target organ to be visualized. This process is not free of artifacts, the principal factors are: body attenuation, scattering, hardware factors, etc. Several studies have shown different ways to correct for body attenuation, scattering and so on, but little effort has been done for the case of patient movement correction. For example, in the case of lungs studies, the breathing cycle affects the quantification of lesions. In [32] the authors investigated the impact of movement during the exam, finding mislocalizations of lesions in the fusion of PET and CT. In [34] they found up to an 34% of lesion volume reduction. Significant tumor motion have been

reported in similar studies [44, 45, 3]. Some studies have been performed in order to correct for breathing movement, they include respiratory gating [34], which synchronize the breathing cycle with the data acquisition process in order to get only data of a specific phase within the breathing cycle, others use respiratory-correlated dynamic PET, where an external FDG source point situated over the patient's thorax correlates with the patient's breathing motion [35]. These techniques have shown improvements in reducing the smearing effects caused by the breathing movement, contributing to a better quantification of lung lesions, in the other hand they either require extra hardware (respiratory gating) or specific data acquisition modes like list-mode data, where not always is possible to have access to this type of data acquisition mode. In this article we provide a methodology that works directly in the accumulated projection set (sinogram), correcting for breathing movement. The method have been tested with phantom images produced with the SimSET simulator and the thorax phantom NCAT.

2 Image Reconstruction Algorithms in Emission Tomography

As it was said, the aim of an image reconstruction algorithm is to obtain from a set of indirect measurements a visual representation of a physical quantity. In Emission Tomography (EM), this physical quantity corresponds to the spatial radiation density, and the indirect measurements correspond to photon counts for every angle, recorded by scintillation detectors. Once the counts are acquired, (i.e., projections) an algorithm is applied to obtain the spatial distribution of the radiation density generated for the radio-isotope which was injected into the patient's bloodstream or inhalated.
These algorithms can be classified in two types; analytical and algebraical. We present a brief description of the most common algorithms that is by no means a complete description of them, but just intended to show a general view.

2.1 Analytical Algorithms

The analytical algorithms are based in an analytical model of the process of acquisition, this model is based on the Radon transform

$$m(t,\theta) \triangleq R\{f\} = \int_{-\infty}^{\infty}\int_{-\infty}^{\infty} f(x,y)\delta(xcos\theta + ysin\theta - t)dxdy \qquad (1)$$

Where $m(t,\theta)$ represents the set of line integrals passing through the object $f(x,y)$. Thus, the problem consists in find $m(t,\theta)$ from $f(x,y)$. Application of inverse FFT doesn't work well because it implies interpolations at high frequencies where the density of the 2D Fourier space is low [1]. The most typical inverse Radon transform algorithm is the Filtered Backprojection algorithm (FBP). It consists of taking each projection profile, take its Fourier Transform (FT), apply a frequency domain filter, take the inverse FT and backproject over the image at the given angle. In emission tomography due to the noisy nature of the data and the incompleteness of the projection data, images reconstructed with FBP suffer from heavy noise. Furthermore, the filtering step amplifies high frequencies, incrementing the noise level. This effect can be decreased applying a window function to the filter but with the need of considering a trade-off between noise level and image resolution due to overlapping

of frequency bands between the true and noise signal. FBP is fast and not hard to implement. However, it oversimplify the data acquisition process considering all measurements equally, which leads to noisy images. In the next section a review of iterative algorithms is presented.

2.2 Iterative Algorithms

Contrary to analytical algorithms, iterative algorithms allow better modellization of the acquisition and emission process. Also, the modelling is discrete and not continuous as in the analytical case (not considering the implememtation). Generally speaking the idea behind consists in, given a set of measurements p and the projection matrix R, find the set of values f that accomplish the relation $p = Rf$. It will be shown later how the matrix R can be constructed and what other type of information can be added to it.
Use of direct algebraical methods to obtain f is not possible due to the large size of the matrix R. Besides, noise in p and the approximation of R doesn't allow an exact solution of f [1]. Furthermore, use of least-squares and pseudo-inverse may deliver negative values.
Algebraical methods overcome these problems using an iterative approach. For every iteration, a projection of the guess image is performed, which is compared, by means of some criteria, with the measured data (i.e., p). The error produced is feedback into the guess image, and a new iteration is performed. The problem with this type of approach is that as the iterations increase the image becomes noisy. This is because the algorithm searches to get f as close as possible to p , which contains noise data. In fact, what is of interest is not the complete data f (true data + noise) but its mean λ. In the next section we review the Maximum-Likelihood Expectation Maximization (MLEM) algorithm which tries to find the mean values of f by means of modelling the data acquisition as a *Poisson* process.

2.3 Maximum Likelihood Expectation Maximization Algorithm

This algorithm, first introduced in emission tomography by Shepp and Vardi [43], is based in a *Poisson* model for the emission process. For a given emission element b the number of emissions f_b follows a Poisson law with mean λ_b

$$f_b \sim Poisson(\lambda_b)$$

Besides, the projection matrix R (or called by some authors *system matrix* or *transition matrix*) gives the probability that a certain emission from pixel b is detected by the detector d (called *dexel* hereafter). Furthermore, the number of detections from dexel d (i.e., p_d) can be calculated as the sum of detections coming from every emission element b

$$p_d = \sum_{b=1}^{b=n} p_{db} \tag{2}$$

Furthermore, the number of detections from emission element b detected by dexel d can be written in function of the number of emissions f_b

$$p_{db} = f_b R_{db} \tag{3}$$

From (2) and (3), the number of detections can be expressed in terms of the number of emissions, as follows

$$p_d = \sum_{b=1}^{b=n} f_b R_{db} \tag{4}$$

Similarly, for the mean counts we can write

$$\overline{p_d} = E[p_d] = \sum_{b=1}^{b=n} \lambda_{db} = \sum_{b=1}^{b=n} \lambda_b R_{db} \tag{5}$$

Where λ_{db} stands for the mean number of emissions from emission element b being detected by dexel d.

The ML estimate searches iteratively to find a value $\hat{\lambda}$ that accomplish the following

$$\hat{\lambda} = \arg\max_{\lambda}[l(\lambda)] \tag{6}$$

with $l(\lambda)$

$$l(\lambda) = P(p|\lambda) \tag{7}$$

the likelihood of getting a set of measures p given the image λ.

To simplify calculations, it is common to employ the log-likelihood, $L(\lambda) = \log[l(\lambda)]$. More important is the fact that the variables λ_{db} are independent variables. Thus, $L(\lambda)$ can be expressed as:

$$L(\lambda) = \log(P(p/\lambda)) = \log\left(\prod_{d,b} e^{-\lambda_{db}} \frac{{\lambda_{db}}^{p_{db}}}{p_{db}!}\right) \tag{8}$$

And equation (6) becomes

$$\hat{\lambda} = \arg\max_{\lambda}[L(\lambda)] \tag{9}$$

In order to solve for (9), maximization of (8) is performed. Taking first derivative of 8

$$\frac{\partial L(\lambda)}{\partial \lambda_b} = \frac{\partial}{\partial \lambda_b}\left(\sum_{d,b} -\lambda_{db} + \log\left(\frac{{\lambda_{db}}^{p_{db}}}{p_{db}!}\right)\right)$$

$$\frac{\partial L(\lambda)}{\partial \lambda_b} = \frac{\partial}{\partial \lambda_b}\left(-\sum_{b}\lambda_b \sum_{d} R_{db} + \sum_{d,b} p_{db}\log(\lambda_b) + C\right)$$

$$= -\sum_{d} R_{db} + \sum_{d}\frac{p_{db}}{\lambda_b} = 0$$

$$\frac{\partial L(\lambda)}{\partial \lambda_b} = 0 \Rightarrow \hat{\lambda}_b = \frac{\sum_d p_{db}}{\sum_d R_{db}} \tag{10}$$

However, since we don't have direct access to p_{db}, it is necessary to calculate its conditional expectation given the measures p_d and the current guess image λ.

Further, remembering that for independent Poisson variables X,Y with means λ_X, λ_Y, the expectation of X conditioned on the sum $X+Y$ is $E[X|X+Y] = \frac{(X+Y)\lambda_X}{\lambda_X+\lambda_Y}$ [43]. The expectation of p_{db} can be calculated as

$$E[p_{db}|p_d, \lambda] = \frac{p_d \lambda_{db}}{\sum_{b'} \lambda_{db'}} = \frac{p_d \lambda_b R_{db}}{\sum_{b'} \lambda_{b'} R_{db'}} \tag{11}$$

Then, substituting equation (11) into (10) we get

$$\lambda_b^{<K+1>} = \frac{\lambda_b^{<K>}}{\sum_d R_{db}} \sum_d \frac{p_d R_{db}}{\sum_{b'} \lambda_{b'}^{<K>} R_{db'}} \tag{12}$$

Where the index K stands for the iteration number.
From (12) we can observe that the algorithm basically follows the same principle already mentioned for the iterative algorithms. It takes a guess image $\lambda^{<K>}$, makes a re-projection of it (denominator in right summation). Then, the ratios between the measured data and the forward-projected values are backprojected into the image space and added. the sum of this values are used as multiplicative update coefficients to iteration $K+1$. The term $\sum_d R_{db}$ acts as a normalization value, as in theory $\sum_d R_{db} = 1$, meaning that every emission should be detected by the system.

The principal characteristics of the MLEM algorithm are its non-negativity (i.e., it assures non-negative pixel values for all the images generated) and, for every iteration the number of emissions equals the number of detections.
One aspect that still remains open is when the iterations should be stopped. Several measures exist that can be used to check the quality of the reconstructed image.
It has been shown [26, 21] that a good figure-of-merit is the Root Mean Square value(RMS)

$$RMS_K = \sqrt{\frac{\sum_b (f_b - \lambda_b^{<K>})^2}{\sum_b f_b^2}} \tag{13}$$

The RMS value shows that in a point in the iterations, its value reaches a minimum and then starts to increase, indicating that noise in the measured

data begins to be added to the reconstructed image [22].
While the RMS value has only utility in simulations studies, where the density distribution can be known a priori, it can not be applied to real studies.
The likelihood of the objective function can be used as a statistical criteria to stop the algorithm:

$$L(\lambda) = \sum_d [p_d \log(\overline{p_d}) - \overline{p_d} - \log(p_d!)] \tag{14}$$

Using equation (5) in (14), the likelihood can be calculated as:

$$L(\lambda) = \sum_d [p_d \log \left(\sum_b \lambda_b R_{db} \right) - \sum_b \lambda_b R_{db} - \log(p_d!)] \tag{15}$$

The problem of using equation (15) is that as the iterations continue, the likelihood will increase (monotonicity of the solution), without indicate the point where noise will begin to be added to the reconstructed image.
In [10], the author presents a new stopping criteria, that consists in separate randomly the projection data in two halves, namely A and B. Then, one proceeds with the reconstruction using the set A, and for each iteration the likelihood of the data set B is calculated using the estimates obtained with A. It is shown that the likelihood will increase until a certain point where the iterations over A are stopped, changing to the data set B. Once both points of convergence are reached, the two estimates are summed up to obtain the final image estimate of the density distribution. This technique has shown good results on noise rejection but as it has been remarked in [19], the cross-likelihood is dependent of the number of counts. In [19], Johnson proposed a variant to the cross-likelihood scheme, in which the projection data set is divided in k subsets. Then, each subset is subtracted from the complete data set. Each subtracted data set is reconstructed and multiplied by $1/(k-1)$ to preserve the counts number in each iteration. For each subtracted data set, the iterations are stopped when the likelihood of the non-included data set is maximized. Other approach has been proposed in [22], where a study of the multiplicative update coefficients of the MLEM algorithm has allowed the authors to establish a stopping rule. For each iteration the update coefficients are stored and histogrammed. The technique is based in the fact that

the optimum iteration value (given in a simulation study by the RMS value) is reached always in the same value for the histogrammed coefficients. In a precedent work [23], the authors stated that a value of 0.8 produces images close to the optimal reconstructed image (with ± 5 iterations).

The MLEM algorithm has shown better results than the classical FBP algorithm, however its inconvenient is its slow convergence. Different approaches has been created to overcome this problem, like parallelism of the process, computational memory management improvements to speed up iterations, and so on. One technique that has improved the speed of convergence and has approached the EM technique to the clinical scenario is the Ordered Subsets Expectation Maximization algorithm (OSEM) [18]. Instead of working with one set of projections, the algorithm performs several sub-iterations over a smaller subset before beginning with the next one. The results using this technique has shown that the image reconstructed gets closer to the convergence point in less time than the original MLEM algorithm. It occurs because for each iteration, a voxel is updated as many times as number of subsets. Therefore, each voxel will be visited more times for iteration than in the case of using a single set of projections. In other terms, for every subset an image is reconstructed considering the information contained in that subset, then, for the successive subsets new information is added to the reconstructed image. The speed up of the algorithm is based on the smaller time required to reconstruct an image with less projection data. According to [18], the higher the number of subdivisions the better level of detail it can be obtained. However, they agree that there is a limit with the number of subdivisions. Beyond this limit, the algorithm lacks of sufficient data to fit the observed data.
Other issue of interest is how to select and how to order the subsets. In [18], the authors remark that the selection of subsets should be done in a balanced way, so that the voxel activity information is also balanced in the subsets [18]. Regarding the order in which the subsets are processed, They suggest that even if the order is arbitrary it is preferable to process subsets which include new information as soon as possible.
Despite the good empirical results presented by OSEM, its major problem has been its lack of proof convergence and ambiguity in the use of priors [1], also it has been stated that it can lead to limit cycles in the iterative object

estinates [17]. Recently, an accelerated convergent ordered subset algorithm was presented [17], that establishes a tradeoff between speed and convergence by using a parameter that updates itself automatically as the iterations proceeds. This parameter introduces a linear combination between the fast but non-convergent OSEM algorithm and the slow but convergent COSEM algorithm [27]. Basically, at the beggining of the iterations more weighting is given to the OSEM image, in order to speed-up the convergence, and then, as the iterations proceeds, more weighting is given to the COSEM image in order to ensure convergence of the global algorithm. The major drawback is that the linear combination needs a precalculation of each guess image (i.e. OSEM and COSEM), which slows the algorithm. The authors stated that this is a point of further research.

3 Incorporating movement correction into the image reconstruction algorithm

How it was said, the correction of movement has been performed mainly by using components attached to the data acquisition system, in an effort of neglecting information that disagree spatially with a static reference, like a CT image, where a fusion of modalities is wanted. Differently, our approach is based in the information of the breathing cycle that can be included in the step of image reconstruction.

Different authors already noticed the convenience of introducing correction factors into the system matrix, like attenuation factors, scattering factors, detector efficiency, etc. This convenience comes from the fact that each element of the system matrix corresponds to the relationship between a given emission element and a detector element. This one-to-one relationship permits the inclusion of these factors in a straightforward way.

To correct for respiratory movement, we have introduced a correction factor that takes into account how an element of emission moves and deforms itself within the respiratory cycle.

In the case of no movement during the data acquisition period, each element of emission will contribute with emissions to a given set of dexels. But, in the presence of movement, it is more likely that the quantity of detections that

each dexel receives will change (even to the point where some dexels will not receive any contribution from the given emission element). Considering this, and remembering that each element R_{db} of the projection matrix represents the probability that an emission from b is detected by dexel d, allow us to correct for movement by recalculating the values of the projection matrix by taking into account the position of every emission element during the data acquisition period. Let's model the movement as a discrete set of time-weighted positions. Then, from equation (12) we can define R^k_{db} as the detection probability of an emission produced by the emission element b and detected by dexel d during the movement state k. Therefore, the new detection probability is:

$$R^C_{db} = \sum_i w_i R^i_{db} \tag{16}$$

Where each $w_i (i = 1, ..., W)$ is a time weight for the state i and W is the total number of discrete positions for our discrete movement model.
The time-weight takes into account the fact that the more time a moving emission element takes over a detection element, the more number of detections this element will capture.
Finally, introducing (16) into (12) we get

$$\lambda_b^{<K+1>} = \frac{\lambda_b^{<K>}}{\sum_d R^C_{db}} \sum_d \frac{p_d R^C_{db}}{\sum_{b'} \lambda_{b'}^{<K>} R^C_{db'}} \tag{17}$$

Equation (16) tries to relocate the number of emissions that due to movement were detected in others dexels but the dexel where they should have been detected in no presence of movement.
The way each term is calculated in equation (16) will take into account the position of the emission element at each state of movement and is calculated as follows

$$R^i_{db} = \frac{l^i_{db}}{\sum_{d'} l^i_{d'b}} \tag{18}$$

Where the term l^i_{db} is the intersection length between the dexel d and the emission element b during movement state i. The summation in the denominator

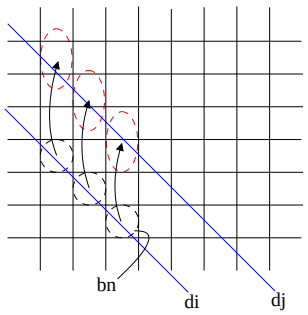

Figure 1: Calculation of system matrix elements considering movement.

of equation (18) acts as a normalization term.
Fig. 1 schematize the way the movement of an emission element will affect the calculation of equation (18). Here, at each grid position, each emission element bn has been modelled as either a circle (2D) or a sphere (3D). Then, in the case of non-movement, the probability $R_{d_i b_n} \neq 0$ and $R_{d_j b_n} = 0$. But if movement comes into play, the situation is the opposite($R_{d_i b_n} = 0$ and $R_{d_j b_n} \neq 0$). Furthermore, as remarked in Fig. 1, not only a displacement of the emission element is been considered but also deformation of it.

3.1 Calculating emission-element volume deformation by diagonalization of Jacobian matrix

As it was said, for the calculation of each system matrix term, not only displacements of each emission element are considered but also volume deformation of it.
Let's be $U(x, y, z)$ the displacement vector field having the information of how an emission element with coordinates (x, y, z) moved in space to the position (x^p, y^p, z^p), and $\varphi(x, y, z)$ the deformation function defined as:

$$\left.\begin{array}{l} x^p = x + U_x(x, y, z) = \varphi_x(x, y, z) \\ y^p = y + U_y(x, y, z) = \varphi_y(x, y, z) \\ z^p = z + U_z(x, y, z) = \varphi_z(x, y, z) \end{array}\right\} \varphi(x, y, z) \tag{19}$$

Then, it is possible to calculate the gradient of $\varphi(x, y, z)$ at a certain emission element $p = (p_x, p_y, p_z)$

$$\nabla_p\varphi = \left(\begin{array}{ccc} \frac{\partial\varphi_x}{\partial x} & \frac{\partial\varphi_x}{\partial y} & \frac{\partial\varphi_x}{\partial z} \\ \frac{\partial\varphi_y}{\partial x} & \frac{\partial\varphi_y}{\partial y} & \frac{\partial\varphi_y}{\partial z} \\ \frac{\partial\varphi_z}{\partial x} & \frac{\partial\varphi_z}{\partial y} & \frac{\partial\varphi_z}{\partial z} \end{array} \right) \Bigg|_{\substack{x=p_x \\ y=p_y \\ z=p_z}} \tag{20}$$

Since $\nabla_p\varphi = Id + \nabla U(x,y,z)$ with Id the identity matrix, equation (20) can be written as:

$$\nabla_p\varphi = \left(\begin{array}{ccc} 1+\frac{\partial U_x}{\partial x} & \frac{\partial U_x}{\partial y} & \frac{\partial U_x}{\partial z} \\ \frac{\partial U_y}{\partial x} & 1+\frac{\partial\ Uy}{\partial y} & \frac{\partial U_y}{\partial z} \\ \frac{\partial U_z}{\partial x} & \frac{\partial U_z}{\partial y} & 1+\frac{\partial U_z}{\partial z} \end{array} \right) \Bigg|_{\substack{x=p_x \\ y=p_y \\ z=p_z}} \tag{21}$$

The value of the determinant of $\nabla\varphi$(a.k.a jacobian of φ) describes if the emission element suffers an expansion ($|\nabla_p\varphi| > 1$), a contraction ($|\nabla_p\varphi| < 1$) or if it preserves its volume ($|\nabla_p\varphi| = 1$) [37]. Moreover, it is possible to calculate in what direction and magnitude the emission element will either expand or contract.

Let's assume that the matrix $\nabla_p\varphi$ is a real symmetric matrix. Then, there exist matrices P and D, such as:

$$\nabla_p\varphi = PDP^{-1} \tag{22}$$

Where, $D = diag(\lambda_p^{(0)}, \lambda_p^{(1)}, \lambda_p^{(2)})$ with $\lambda_p^j (j = 0,1,2)$ eigenvalues of $\nabla_p\varphi$ and each column of matrix P, an eigenvector of matrix $\nabla_p\varphi$. What is of our interest, is the information that can be retrieved from matrices P and D.

Since the eigenvectors represent the preferred directions of a matrix, in our case they represent the preferred deformation direction of an emission element, whilst every eigenvalue gives the magnitude of the deformation in the direction of the associated eigenvector.

Fig. 2 presents a test performed to check how emissions elements (modelled as spheres) translate and change their volume according to a pre-built displacement vector field.

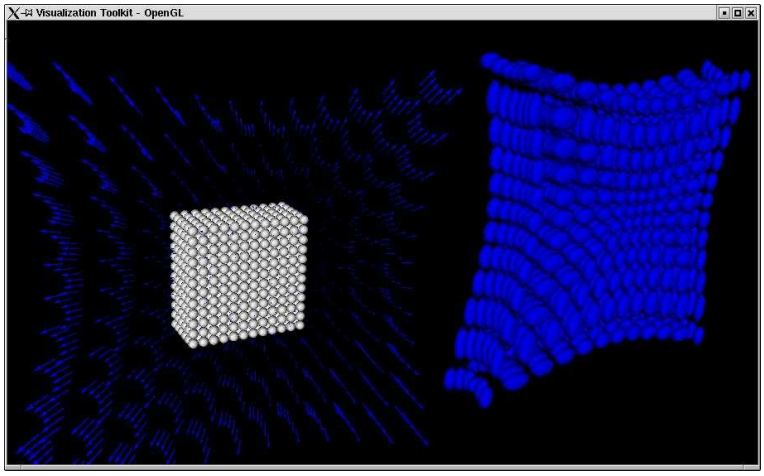

Figure 2: Testing the deformation of a set of sphere-shape-modelled emissions elements following a pre-built displacement vector field. Left: Original set and displacement vector field. Right: Translated and deformed set.

4 Implementation

This section presents the implementation issues concerning the parallelization of the MLEM algorithm as well as the accelerators for the forward and backward operators. To finalize with a brief description of the SimSET library and the NCAT thorax phantom, utilized for the lungs simulation.

4.1 Parallelization of the MLEM algorithm for 3D image reconstruction

In section 2.3, it has been remarked the slow convergence of MLEM, and some solutions were presented in order to decrease the convergence time. While in two dimensions the speed problem of the technique is feasible to solve by using for example smaller projections subsets at each iteration (OSEM approach) or by designing more complex ways to store the system matrix to gain faster data access times. In three dimensions it is required a force brute method like parallelism.
Parallelization of EM algorithms has been already used to speedup the con-

vergence, in [21] a summary of previous works is described. Here the common denominator has been the distribution of the computational load of forward and backward projections over a set of processors.
The main aspect of the algorithm in terms of parallelization, is without a doubt the independence between neighbor emissions elements over a single iteration, which eases its implementation.
Our implementation is composed by three stages of parallelism. First, as suggests equation (16), calculus of the normalization term for the corrected detection probability should be yielded before the steps of forward and back projection. Then, parallelization of forward projection step is performed. The counts estimates are stored and used in the next and final step of parallelization; backward projection and image update.
Fig. 3 shows a diagram where it can be seen how each one of this parallelization tasks relates to the others. Each box in Fig. 3 represents an entity of

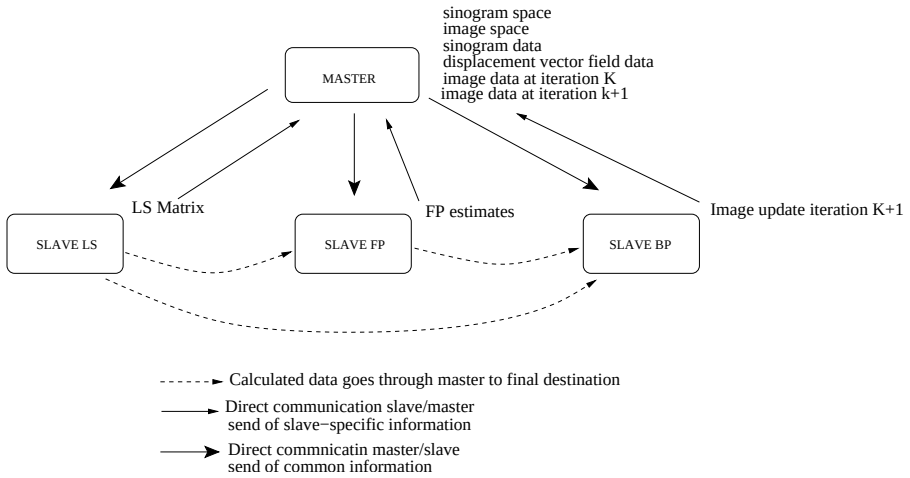

Figure 3: Implementation diagram of parallelized MLEM algorithm.

execution, starting by the master that makes the light calculations (i.e., calculating the sinogram and image space dimensions, reading the sinogram data file, initializing the image to be reconstructed, etc.). The first slave created is *SlaveLS*, which calculates the normalization term in equation 16. Once the slave has finished its task, it sends the data back to the master, which store it to be used later for the two other slaves. The second slave, *SlaveFP*, is in

charge of the forward projection part (i.e., right denominator in equation 17). Besides from the basic information delivered by the master, it receives the already calculated normalization term. The detection count estimates are sent back to the master, which will spawn the last set of slaves that perform the back-projection operation. Once again, the data calculated in the previous steps is sent to every *SlaveBP*. Once the *SlaveBP* has finished its work, it sends the portion of the updated image estimate to the master, which gets the data from each slave and assembles the image. At this point an iteration is completed.
For the communication between master and slaves, the *PVM (Parallel Virtual Machine)* software was used [11] and execution was performed in the INRIA Sophia Antipolis cluster system [15].

4.2 Accelerating the MLEM using geometrical considerations

Geometrical considerations can be used to diminish the number of calculations in equation (12). Specifically in the two more computationally expensive operations: forward and backward projection. For the former, the first approach was to calculate a region of interest that takes into account the geometrical space traversed by a specific dexel (see Fig. 4). Later, the well-known Bresen-

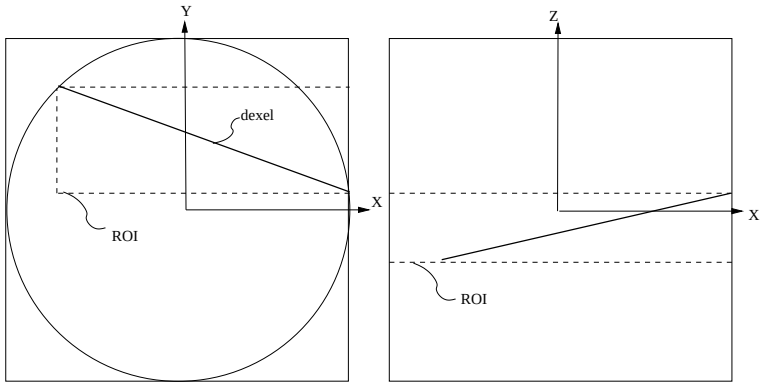

Figure 4: Region of interest to reduce calculation times in forward projection.

ham's algorithm [5][50] used to represent a continuous line in a discrete space

was incorporated as a better accelerator. While the goal of the Bresenham's algorithm is to better represent a continuous line over a grid space, sometimes it fails in adding all the pixels (2D case) traversed by the line. Which in our case is of vital importance in order to take into account all voxels contributing to a specific dexel. Then, for each voxel given by the Bresenham's algorithm (3D version), a 6-neighborhood was considered to ensure that the voxels traversed by the dexel are present. Fig. 5 shows the result from the implementation of the 3D Bresenham's algorithm with the previously mentioned 6-neighborhood.

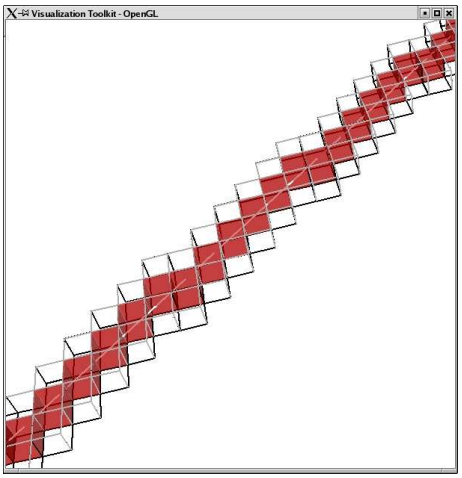

Figure 5: Bresenham 3D with 6-neighboring to accelerate forward projection. The red cubes, are the ones from the 3D bresenham's algorithm, and the others are the 6-neighbors for each of the red cubes. This, to ensure that all voxels traversed by the dexel are included.

To accelerate the backward projection step, at every voxel an angle-specific forward projection operation is performed to get a list of dexels passing trough it. Formerly, for a given emission element b, the non-accelerated backward projection operation consists on calculate:

$$\sum_{d} \frac{n_d p_{db}}{\widetilde{n}_d}; \forall\ d \in D \tag{23}$$

With D the set of all dexels forming the scanner system and $\widetilde{n}_d$ the current estimated value for emissions detected by dexel d. As not all dexels d will traverse emission element b (yielding null probabilities p_{db}). It is possible to reduce the set of dexels to be visited by applying a forward projection operation to the emission element b at every azimuthal angle $\theta_i, i = 1, ..., n$.

$$D' = [F_{\theta_1}(b), ..., F_{\theta_n}(b)] \tag{24}$$

Where, $F_\theta(b)$ stands for the forward projection operator applied to emission element b at angle θ. Finally, the backward projection operation of emission element b over the reduced set D' will be

$$\sum_{d'} \frac{n_{d'b} p_{d'b}}{\widetilde{n_{d'}}}; \forall\ d' \in D' \tag{25}$$

The previous procedure is depicted in Fig. 6 where continuous lines represent dexels in reduced set D' and non-continuous lines are examples of dexels being discarded from set D'.

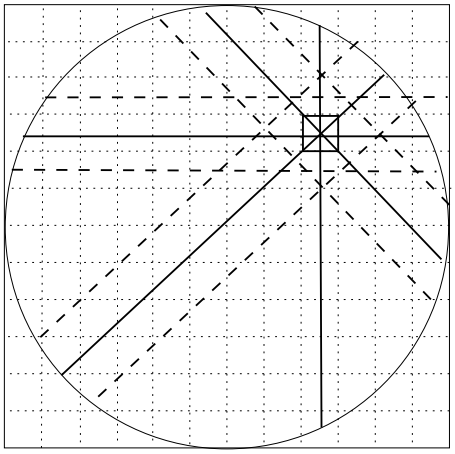

Figure 6: Reducing dexel space in backward projection. Continuous lines represent the dexels that are being considered for the forward projection while non-continuous lines are not included in the forward projection step.

If movement correction will be incorporated, it is necessary to include it in the acceleration steps. As it was said for the forward projection step, the Bresenham's algorithm was used to obtain a speed-up. This speed-up is basically

due to the smaller set of emission elements used in the estimation of outcomes. In the presence of movement, the emission elements contributing to a specific dexel during movement have to be added to the set of emission element given by the Bresenham's algorithm.
Formerly, for dexel d, the set B of emission elements to be considered during forward projection is:

$$B = Bresenham(d) \cup \bigcup_i P^i(d), i = 1, ..., W$$

Where $Bresenham(d)$ is the set of emission elements given by the Bresenham's algorithm and

$$P^i(d) = \{b_j, \forall j / l^i_{db_j} \neq 0\}$$

Similarly, for the back-projection step the presence of movement should be taken into account. Revisiting equation (24) and (25), we can recalculate the set of dexels passing through a specific emission element by considering the states of movement. Then, equation (24) can be rewritten as:

$$D' = \bigcup_i [F_{\theta_1}(T^i(b)), ..., F_{\theta_n}(T^i(b))], i = 0, ..., W \tag{26}$$

with $T^i(b)$ the transformation that gives the position of emission element b in movement state i.
The ML-EM algorithm was implemented and tested with synthetic images generated with the SimSET library, which is briefly described in the next section.

4.3 Using the SimSET library to simulate emission tomography

The *Simulation System for Emission Tomography*(SimSET), is a library that simulates the process of emission tomography allowing the configuration of several components, going from the physical to the instrumentation process. Fig.7 shows these components.

The principal modules are the *Object Editor*, in which is possible to create

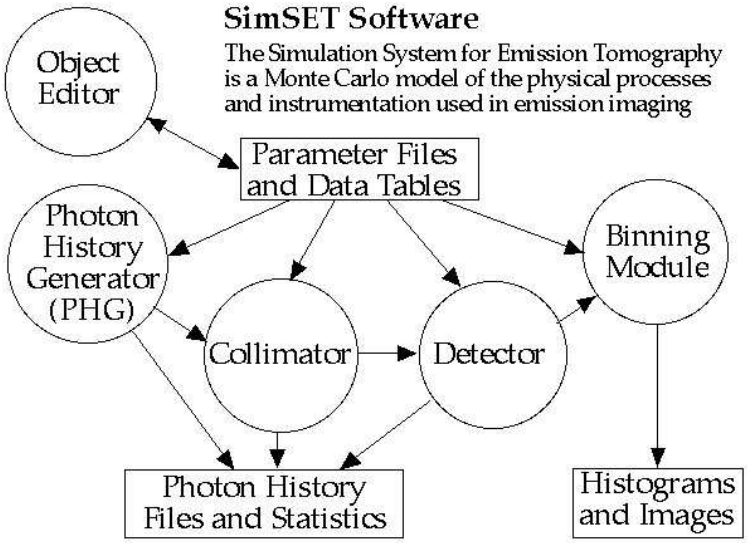

Figure 7: The SimSET library modules.

activity and attenuation objects (using basic geometrical forms). The *Photon History Generator*, that creates and follows the photons through the different layers of the simulation. Finally, The tracked photons can be passed to the *Binning Module* which generates the sinogram data file (among others formats).

Through a command line it is possible to generate the activity and attenuation objects. In addition, the library has the flexibility to allow the use of pre-existing image data (e.g., phantoms). By means of a series of questions, SimSET collects the necessary information to read this data.

The *Photon History Generator* is configured using a text file, in which several options can be set, like number of decays to simulate, whether to simulate SPECT or PET, initial photon energy, simulation time, pointers to the already generated activity and attenuation files, effective field of view of the simulation etc.

Once the configuration is done, the simulation can be executed. Several features can be retrieved from the photons detected (e.g, binning according to energy level, binning according to scattering history, setting of format pre-

cision, etc.). In our case, we are interested in the generated sinogram data file, which sorts the detected photons based on the transaxial distance and azimuthal angle.
For more details of the SimSET library, the authors suggest the reader the citations [16, 49].

4.4 Using the NCAT phantom to simulate emission tomography in human lungs

In order to reproduce the breathing movement in emission tomography simulations, a thorax phantom called *NCAT phantom* has been used.
NCAT, stands for *NURBS-based cardiac torso* and was developed by P. Segars [41]. It is a model of the human thorax anatomy and physiology created primarily for the nuclear medicine imaging research. The fourth dimensionality of the phantom allows modelling of the heart beating and respiratory motions, which is of our primary interest.
Different states within the breathing cycle were acquired and passed as input data to the SimSet library. Then, the obtained sinograms were combined to simulate movement during the data acquisition. In the next section it is explained how this respiratory movement information is utilized in the image reconstruction algorithm.

5 Results

To test for movement correction, several tests were performed. Starting by a simple 2D sphere-shape object, where correction of translation and deformation of the object was achieved. Followed by 2D and 3D simulations of human lungas with simulated respiratory movement. To finalize with a 3D simulation of a small lesion added to the lungs to test for movement correction over a small structure.

5.1 Movement correction applied to 2D synthetic images

Synthetic 2D images simulating a radioactive rod was created, which translates a known magnitude. These activity objects were used in a SimSET simulation to simulate photons decay. Then, the obtained sinograms (i.e. reference state and translated state) were averaged to obtain a final sinogram which simulates an instantaneous translation of the radioactive rod.
Fig. 8 shows the reconstruction obtained by applying MLEM without any movement correction.
From Fig. 8 it is clear to see that MLEM has reconstructed an image com-

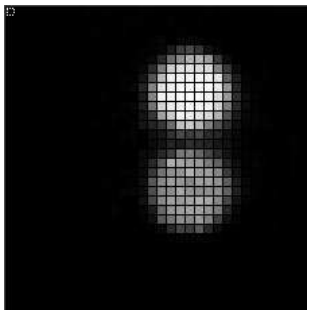

Figure 8: Reconstruction of a moving radioactive rod without movement correction.

posed by the two states. Now, as the displacement field is known (a simple translation), it is possible to apply the algorithm with movement correction. The result is shown in Fig. 9. Fig. 9 shows how the movement correction technique has successfully corrected the spatial activity of the simulated rod.

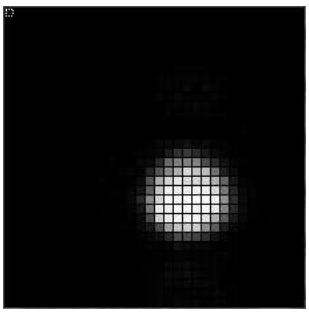

Figure 9: Reconstruction of a moving radioactive rod with movement correction.

Figure 10: Reconstruction of a linearly deforming radioactive rod without movement correction.

Next, correction of a deforming rod was also achieved. To simulate this situation, the rod was deformed linearly in one direction, then the same procedure applied for the case of the translating rod was applied. Fig. 10 shows the reconstruction obtained without correction.
Fig. 10 shows clearly how the deformation adds to the reconstructed image a fuzzy region in the upper border of the rod. Later, the same effect could be compared with the fuzzy zone produced in the frontal region of the human lungs during simulated breathing.

The applied displacement vector field can be used to correct for movement, whose result is shown in Fig. 11
The result obtained shows an improvement in the reconstruction, in terms of density reduction in pixels where no activity should appear in a free-movement

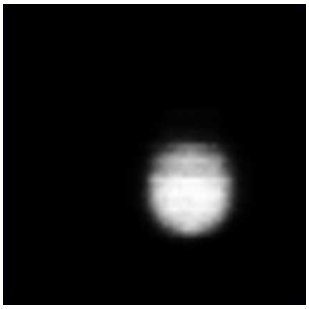

Figure 11: Reconstruction of a moving radioactive rod with movement correction.

image reconstruction. Nonetheless, there are some artifacts in the corrected image. Our assumption is that during the image reconstruction with movement correction a discretization in the inverse application of the displacement vector field caused some pixels to present more density than others.

To be more realistic, the NCAT phantom was used. First as a 2D phantom and then as a 3D one. For the former, two states of the respiratory cycle were taken (namely full-inspiration and full-exhalation). Then, SimSET simulations were performed and sinograms were combined to simulate breathing during the emission tomography exam. For the posterior reconstruction with movement correction, the displacement vector field was calculated by using a non-rigid registration algorithm called Pasha [6].
From Fig. 12 it can be noticed that lungs deformation occurs mainly in the upper region, while the deformation in the posterior part is smaller. From the combination of both projections sets, simulation of breathing was achieved. As in the case of Fig. 10, it is expected that a fuzzy region should appear in the frontal region. However, since it is less notorious than the case of the deformed radioactive rod, the results in the application of the movement correction is better visualized in terms of image-differences between the two states of movement used in the simulation. Fig. 13 shows (a)the resulted reconstructed image and (b)the result of subtracting the non-corrected image and the reference image (i.e., full-expiration).

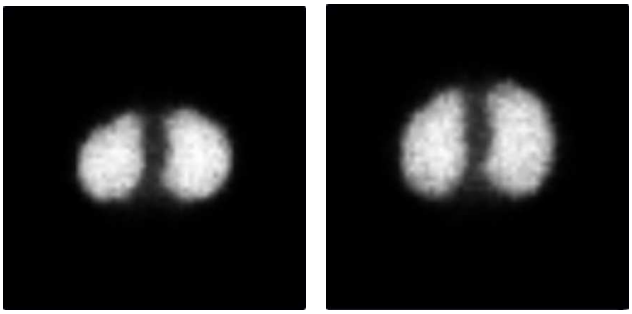

(a) Full-Expiration (b) Full-Inspiration

Figure 12: Image reconstruction of (a)full-expiration and (b)full-inspiration states.

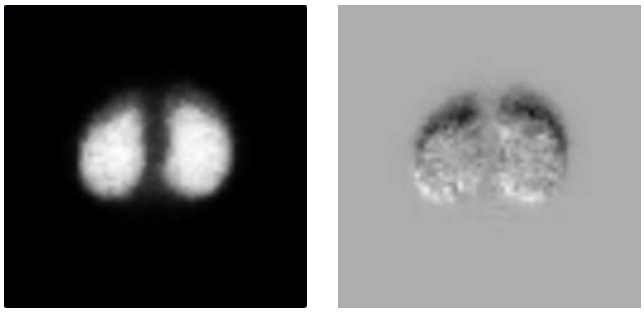

(a) Simulation of breathing during the emission tomography exam.

(b) Image difference between the non-corrected reconstructed image and full-expiration.

Figure 13: (a) Image reconstruction of two combined states of the respiratory cycle, (b) Image-difference between non-corrected image and reference image.

As it was expected, from Fig. 13, a fuzzy region is visible in the frontal part of the lungs. The movement correction was performed by using the displacement vector field obtained from the non-rigid registration between the two states of movement. Fig. 14 shows the result obtained, the displacement vector field used in the correction step and the image difference between the movement corrected image and the full-expiration image, which is our reference. From

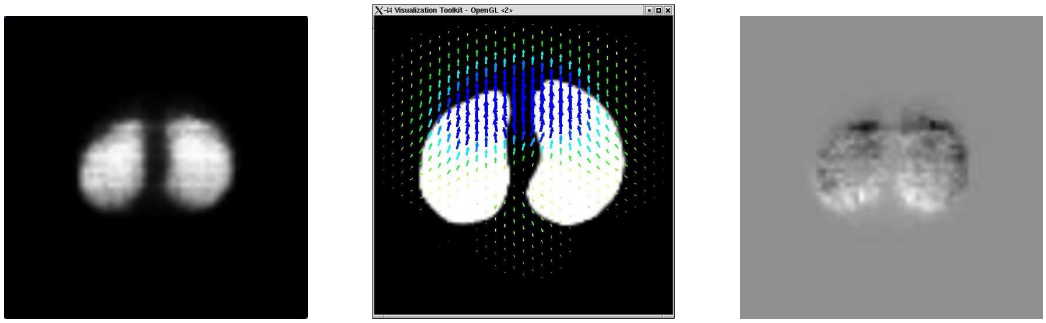

(a) Image reconstruction with movement correction of simulated breathing.

(b) Displacement vector field.

(c) Image difference of corrected image and full-expiration state (reference).

Figure 14: (a)Image reconstruction with movement correction of two combined states of the respiratory cycle, (b) displacement vector field obtained from registration of full-expiration and full-inspiration states, (c)Image difference of corrected image and full-expiration state (reference).

Fig. 14 it can be seen that application of the movement correction technique has decreased the fuzzy region produced by the expansion of lungs during inspiration.
To better compare the results, a thresholding can be applied to both image-difference images, which is shown in Fig. 15.

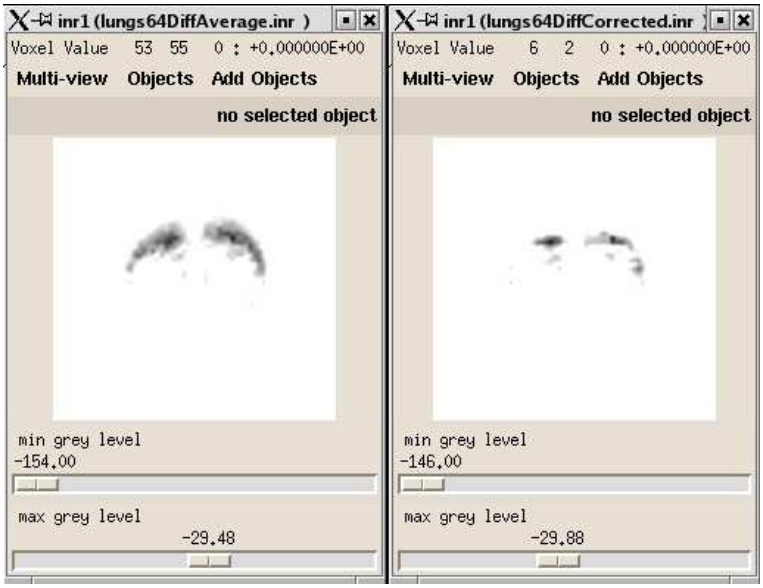

Figure 15: Comparison of corrected and non-corrected image, by means of thresholding image-differences.

5.2 Movement correction applied to 3D images

To test for movement correction in volumetric images, a similar procedure used in 2D was performed. First, from the NCAT phantom, a volumetric dataset corresponding to the state of full-expiration was extracted. This dataset was deformed using a pre-built displacement vector field. This step differs from the 2D case, where the displacement vector field used in the correction was calculated by using a registration algorithm, which can introduce errors to the movement correction step, whereas our primary objective at this point was to check the movement correction technique. Fig. 16 shows 3D isosurfaces of full-expiration and the deformed volume (rendered with transparency). Besides, the displacement vector field has been included as arrow glyphs.

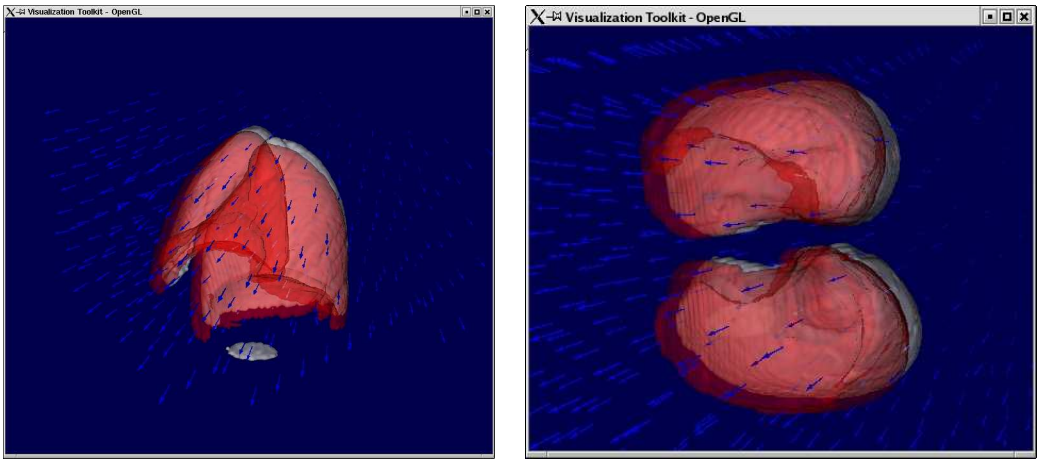

Figure 16: Full-expiration and deformed volume (in transparent red) isosurfaces and displacement vector field.

Each volumetric dataset of dimensions 64x64x64 underwent a SimSET simulation. Then, the obtained sinograms were combined to simulate movement during the data acquisition process.
The MLEM reconstructions were performed with the parallel architecture presented in section 4.1. In order to compare results in a qualitative way, meshes were generated for the reconstructed reference volume (i.e., full-expiration

state) and for the non-corrected and corrected reconstructed volumes. Then, for each point in the reference surface its corresponding closest point in the normal direction, in the non-corrected and corrected surface was found, and the distance between these two points was calculated. In this way for the non-corrected and corrected images a distance map was obtained. Fig. 17(a) shows the distance map obtained between the reference and the non-corrected reconstructed image and Fig. 17(b) shows the distance map obtained using the movement corrected image.

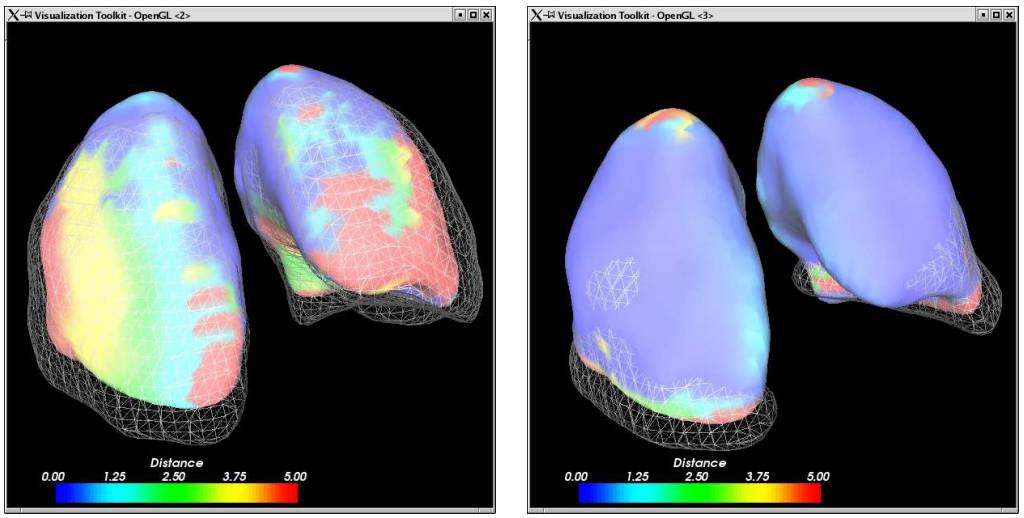

(a) non-corrected (b) corrected

Figure 17: Non-corrected (a) and corrected color distance map (b) obtained from calculating the distance between each point in the reference image (full-expiration) and the closest point in the normal direction to it. In wireframe representation it is shown the non-corrected (a) and corrected (b) meshes.

From Fig. 17, it can be seen how the distance values between meshes are mapped into the original one, going from low values (blue) to high values (red). It can be seen from Fig. 17(b) how the movement correction technique has produced low distance values (w.r.t the reference image), indicating a better image reconstruction. Nonetheless, the corrected image presents a higher

distance values at the bottom of the lungs, which is investigated to be a border condition problem. It is important to remember that since the generated meshes come from an iso-surfacing algorithm, the qualitative criteria of the correction method will depend on the isovalue selected to create the surfaces. However, despite this issue, the qualitative method helps to visualize in some degree (depending on the isovalue) the correction achieved by the technique. Next, a spherical lesion with a radius of 1cm was added in order to test the movement correction over a small structure inside the lungs. Fig. 18 shows the activity image for the reference state.

(a) sagittal plane (b) axial plane (c) coronal plane

Figure 18: activity image including of lungs and a simulated lesion. The lesion is modelled as a sphere with a radius of 1cm.

The activity images of Fig. 18 were deformed with the displacement vector field showed in Fig. 16 to produce a deformed state similar to that of full-inspiration. Then, SimSET simulations and combination of sinograms were performed to get a sinogram which simulates respiratory movement. This sinogram underwent MLEM iterations with and without movement correction. To test the results obtained in the movement correction of the lesion, the qualitative method, showed previously for the lungs surfaces, was utilized. The isosurfaces were generated using a threshold obtained visually from the reconstructed images. Fig. 19 shows the distance maps between the non-corrected mesh (Fig. 19(a)-(c) wireframe representation) and corrected mesh (Fig. 19(b)-(d) wireframe representation) with reference mesh of the lesion.

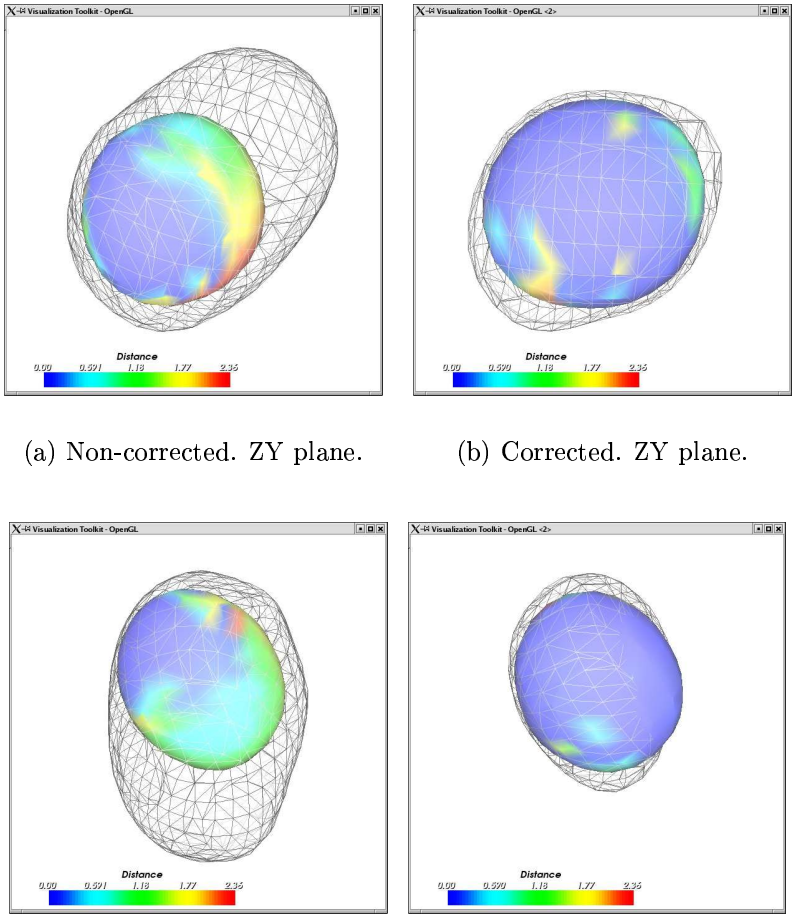

(a) Non-corrected. ZY plane. (b) Corrected. ZY plane.

(c) Non-corrected. XZ plane (d) Corrected. XZ plane

Figure 19: Qualitative test of movement correction for lesion in Fig.18.

As shown in Fig. 19, the movement correction methodology has clearly improved the spatial distribution of the activity in the lesion. However, as it was stated, the qualitative method depends on the segmentation of the structure of interest. Moreover, as in this case the structure corresponds to a small volume, sensitivity in the step of isosurfacing is higher. Therefore, the qualitative test is not enough to measure the quality of the results obtained and thus, it should be used in conjunction with other method. For this, profiles of intensity were generated to compare among reference, non-corrected and corrected profiles. Fig. 20 shows profiles of axial slice 43 along its abscise.
and Fig. 21 shows the evolution of the movement correction along iterations of the MLEM algorithm. It can be seen from Fig. 21 how the corrected profile gets close to the reference profile with the increase of MLEM iterations. Also, it can be noticed that as we get close to the reference (or as the iterations proceeds) it is necessary more iterations to improve the correction. This result was expected since the technique applies a count-estimate repositioning using the movement information, but as the count-estimates are being "improved" at each iteration, then the repositioning of these estimations will also improve at each iteration.
Concerning the speed-up obtained by the parallelization of the algorithm and the forward and backward accelerators, Fig. 22 shows a plot of speed-up in function of the number of processors.
Figure 23 shows a bar plot of time repartition for the principal inter-iteration tasks as communication master-slave, forward projection, backward projection and system matrix normalization. For one iteration of a 64^3 volume and a 64^3 sinogram data. It can be seen from Fig. 23, that the time spend in communication increase as the number of processors increase, this result is expected since a synchronous communication type has been used. Further, the more number of slaves are specified, the less time the three main process will take, but with the inconvenient that the communication time will increase and it will get proportions comparable to those of forward and backward projection (e.g,. number of slaves =12 in Fig. 23), which should be readapted if independence between communication time and the number of slaves is required. However, the selection of the number of slaves should be done considering the size of the data to be reconstructed.

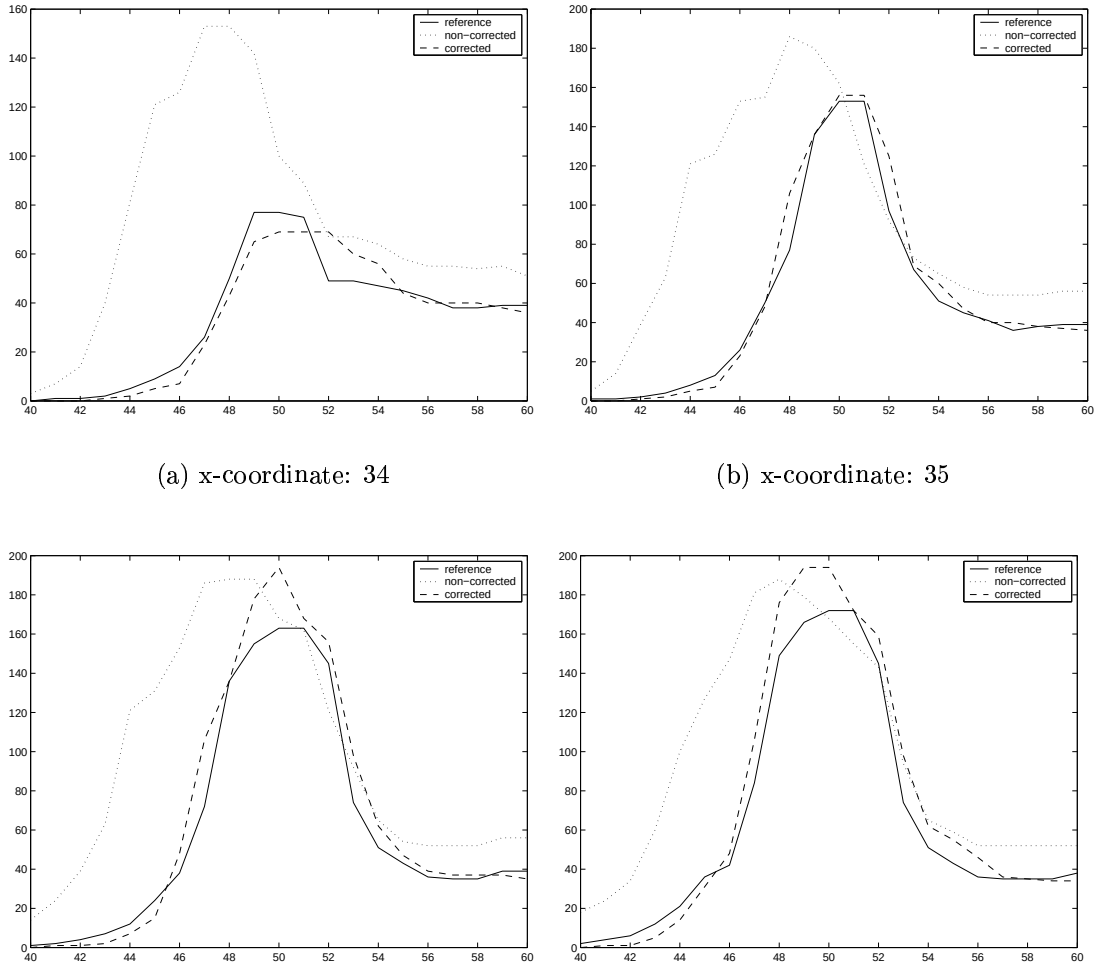

(a) x-coordinate: 34

(b) x-coordinate: 35

(c) x-coordinate: 36

(d) x-coordinate: 37

Figure 20: Intensity profiles for axial slice 43 around the lesion area. After 20 MLEM iterations the corrected profiles show a close relationship with the reference profiles.

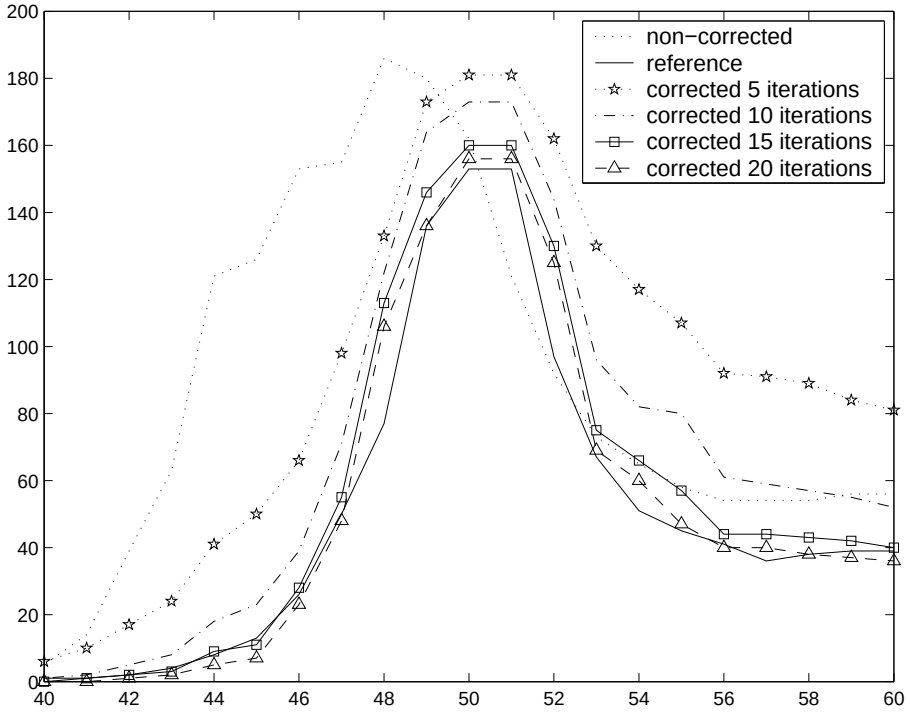

Figure 21: Evolution of movement correction in the lesion area.

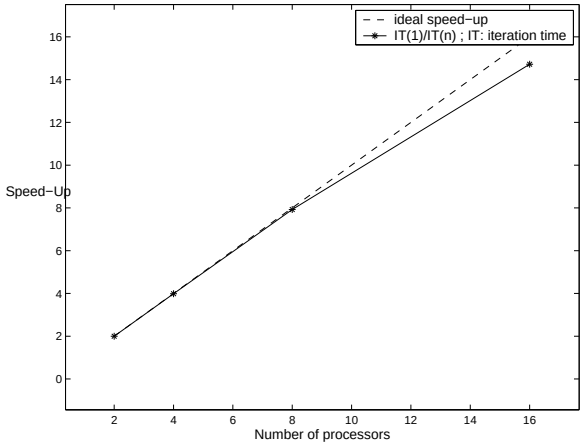

Figure 22: Speed-up in function of the number of processors for the parallel implementation of the MLEM with movement correction algorithm

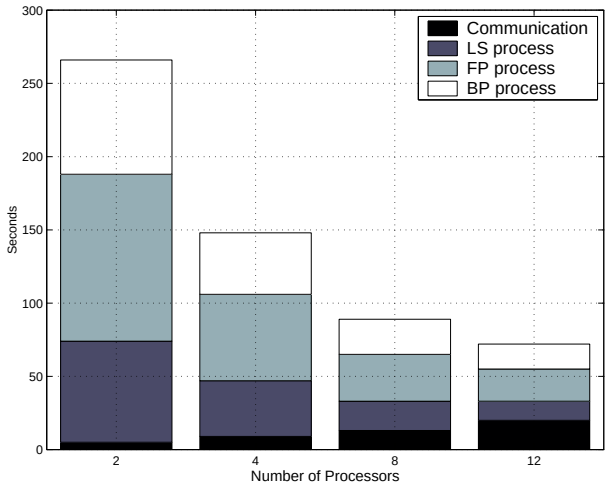

Figure 23: Time repartition for communication time, LS process (normalization term for each term of the matrix system), FP process (forward projection) and BP (backward projection) for a single iteration and in function of the number of slaves.

6 Conclusions

Induced motion due to patient breathing during an emission tomography exam can leads to artifacts in the reconstructed image, artifacts that can produce less accurate diagnosis and more important, incorrect radiotherapy planning [33][34][42]. Here, we have presented a methodology to correct for respiratory movement in the image reconstruction step. By modifying the way the system matrix is calculated, it was possible to us to add information about the respiratory movement into the reconstruction algorithm. Furthermore, volume deformation of the emissions elements was taken into account, where an emission element can suffer not only a translation during the breathing cycle but also a deformation.

Considering Figs. 20 and 21, the movement correction is an iterative process, which goes attached intrinsically to the evolution of the MLEM algorithm itself. In this sense it would be interesting to follow studies in the use of weighting schemes to accelerate the movement correction procedure (as it has been used for algebraical algorithms like ART and MART).

The 2-D and 3-D simulations yielded good results, encouraging the application of this methodology to real data. However, since the efficacy of the method is based on the certitude degree of knowing the movement produced during the exam, it will be important to consider a breathing model allowing a good fit with the breathing cycle of the patient. In this sense a parametric respiratory model is expected to be used.

Concerning implementational issues, parallelization of the algorithm and accelerators to the steps of forward and backward projection were presented. The Bresenham's algorithm, a classical algorithm in computer graphics, was used successfully in the task of accelerating the forward projection step, which, until our knowledge, presents a novel contribution to the speed-up of the algorithm. Both, parallelization of the algorithm and the accelerators presented, were crucial in the implementation of the MLEM-3D to get iterations times of the order of some minutes. This can be an important factor if we think in incorporation of the technique in a clinical scenario.

References

[1] S. Alenius. *On Noise Reduction in Iterative Image Reconstruction Algorithms for Emission Tomography: Median Root Prior.* PhD thesis, Tampere University of Technology, 1997.

[2] John A.D Aston, Vincent J. Cunningham, Marie-Claude Asselin, Alexander Hammers, Alan C. Evans, and Roger N. Gunn. Positron emission tomography partial volume correction: Estimation and algorithms. *Preprint of JCBFM*, August 2002.

[3] JM. Balter, RK. Ten Haken, TS. Lawrence, KL. Lam, and JM. Robertson. Uncertainties in CT-based radiation therapy treatment planning associated with patient breathing. *International Journal of Radiation Oncology, Biology, Physics.*, 36(1):167–74, 8 1996.

[4] M. Betke, H. Hong, and J.P. Ko. Automatic 3D registration of lung surfaces in computed tomography scans. In W.J. Niessen and M. A. Viergever, editors, *Medical Image Computing and Computer-Assisted Intervention MICCAI'2001*, volume 2208, pages 725–733, Utrecht (Netherlands), 2001. Springer Verlag, Lecture Notes in Computer Science.

[5] J.E. Bresenham. Algorithm for computer control of digital plotter. *IBM Systems Journal*, 4(1):25–30, January 1965.

[6] P. Cachier, E. Bardinet, D. Dormont, X. Pennec, and N. Ayache. Iconic Feature Based Nonrigid Registration: The PASHA Algorithm. *CVIU — Special Issue on Nonrigid Registration*, 89(2-3):272–298, Feb.-march 2003.

[7] J. Cai, JC. Chul, D. Recine, M. Sharma, C. Nguyen, R. Rodebaugh, VA. Saxena, and A. Ali. CT and PET lung image registration and fusion in radiotherapy treatment planning using the chamfer-matching method. *Int. Journal of Radiation Oncology, Biology, Physics*, 43(4):883–91, Mar 1999.

[8] O. Camara, G. Delso, and I. Bloch. Evaluation of a thoracic elastic registration method using anatomical constraints in oncology. In *2nd. Joint*

Conference of the IEEE Engineering in Medicine and Biology Society, 2002.

[9] O. Camara, G. Delso, V. Frouin, and I. Bloch. Improving thoracic elastic registration in oncology by using anatomical constraints. In *Medical Imaging, Understanding and Analysis (MIUA)*, 2002.

[10] K.J. Coakley. A cross-validation procedure for stopping the EM algorithm and deconvolution of neutron depth profiling spectra. *IEEE Transactions on Nuclear Medicine*, 38(1):9–15, February 1991.

[11] A. Geist, A. Beguelin, J.J. Dongarra, W. Jiang, R. Manchek, and V.S. Sunderam. PVM 3 user's guide and reference manual. Technical Report ORNL/TM-12187, Oak Ridge National Laboratory, 1993.

[12] G.W. Goerres, C. Burger, M.R. Schwitter, T.-N. H. Heidelberg, B.Seifert, and G.K. von Schulthess. PET/CT of the abdomen: Optimizing the patient breathing pattern. *European Radiology Published Online First*, 2002.

[13] G.W. Goerres, E. Kamel, T.-N. H. Heidelberg, M.R. Schwitter, C. Burger, and G.K. von Schulthess. PET-CT image co-registration in the thorax:influence of respiration. *European Journal of Nuclear Medicine*, 29:351–360, 2002.

[14] G.W. Goerres, E. Kamel, B. Seifert, C. Burger, A. Buck, T.F. Hany, and G.K. von Schulthess. Accuracy of image coregistration of pulmonary lesions in patients with non-small cell lung cancer using an integrated PET/CT system. *J. Nucl. Med*, 43(11):1469–75, 2002.

[15] Parallel computing at INRIA sophia-antipolis: a cluster computing approach. http://www-sop.inria.fr/parallel/.

[16] RL. Harrison, SD. Vannoy, DR. Haynor, SB. Gillispie, MS. Kaplan, and TK. Lewellen. Preliminary experience with the photon history generator module of a public-domain simulation system for emission tomography. *Conf. Rec. IEEE Nucl. Sci. Symp.*, pages 1154–1158, 1993.

[17] Ing-Tsung Hsiao, Anand Rangarajan, Parmeshwar Khurd, and Gene Gindi. An accelerated convergent ordered subsets algorithm for emission tomography. *Phys. Med. Biol. 49 (7 June 2004) 2145-2156*, 49(7):2145–2156, June 2004.

[18] H.M. Hudson and R.S. Larkin. Accelerated image reconstruction using ordered subsets of projection data. *IEEE Transactions on Medical Imaging*, 13(4):601–609, 1994.

[19] V.E. Johnson. A note on stopping rules in EM-ML reconstructions of ECT images. *IEEE Trans. Med. Imag., Correspondence*, 13(3):569–571, Sept. 1994.

[20] G.J. Klein, B.W. Reutter, E.H. Botvinick, T.F. Budinger, and R.H. Huesman. Fine-scale motion detection using intrinsic list mode PET information. In *MMBIA01*, pages 71–78, 2001.

[21] G. Kontaxakis. *Maximum likelihood image reconstruction for positron emission tomography: Convergence characteristics and stopping rules.* PhD thesis, Rutgers University, 1996. 240 p.

[22] G. Kontaxakis and G. Tzanakos. Study of the convergence properties of the EM algorithm - a new stopping rule. *IEEE Nucl. Sci. Symp. and Med. Imag. Conf.*, 2:1163–1165, November 1992. Orlando, FL, USA.

[23] G. Kontaxakis and G. Tzanakos. Practical application of a new stopping criterion for the EM-MLE image reconstruction for PET. *Proceedings of the 18th IEEE-EMBS Annual International Conference*, 2:848–849, November 1996.

[24] C. Labbe, JC. Froment, A. Kennedy, J. Ashburner, and Cinotto. Positron emission tomography metabolic data correction for cortical atrophy using magnetic resonance imaging. *Alzheimer Dis and Assoc. Disord.*, 10(S2):141–170, 1996.

[25] H. Lester and S.R Arridge. A survey of hierarchical non-linear medical image registration. *Pattern Recognition*, 32(1):129–149, 1999.

[26] E Levitan and G. Herman. A maximum a posteriori probability expectation maximization algorithm for image reconstruction in emission tomography. *IEEE Trans. Med. Im.*, 6(3):185–192, Sept 1987.

[27] R. Levkovitz, D. Falikman, M. Zibulevsky, A. Ben-Tal, and A. Nemirovski. The design and implementation of COSEM, an iterative algorithm for fully 3-D listmode data. *IEEE Trans Med Imaging*, 20(7):633–42, July 2001.

[28] H. Loats. CT and SPECT image registration and fusion for spatial localization of metastatic processes using radiolabeled monoclonals. *J. Nucl. Med.*, 34:562–566, 1993.

[29] F. Maes, A. Collignon, D. Vandermeulen, G. Marechal, and R. Suetens. Multimodality image registration by maximization of mutual information. *IEEE Tans. Med. Imag.*, 16(2):187–198, april 1997.

[30] D. Mattes. Automatic multimodality image registration with deformations. Master's thesis, Univ. of Washington Medical Center, Seattle, 2000. Technical report, thesis for the degree of MS in Electrical Engineering.

[31] A. Matthies, M. Hickeson, A. Cuchiara, and A. Alavi. Dual time point 18F-FDG PET for the evaluation of pulmonary nodules. *J. Nucl. Med.*, 43(7):871–5, 2002.

[32] MM.Osman, C. Cohade, Y. Nakamoto, LT. Marshall, JP. Leal, and RL. Wahl. Clinically significant inaccurate localization of lesions with PET/CT: frequency in 300 patients. *J. Nucl. Med.*, 4(2):240–243, 2003.

[33] MM.Osman, C. Cohade, Y. Nakamoto, and RL. Wahl. Respiratory motion artifacts on PET emission images obtained using ct attenuation correction on PET-CT. *J. Nucl. Med.*, 30(4):603–6, 2003.

[34] SA. Nehmeh, YE. Erdi, CC. Ling, KE. Rosenzweig, H. Schroder, SM. Larson, HA. Macapinlac, OD. Squire, and JL. Humm. Effect of respiratory gating on quantifying PET images of lung cancer. *J. Nucl. Med.*, 43(7):876–81, 2002.

[35] SA. Nehmeh, YE. Erdi, KE. Rosenzweig, H. Schroder, SM. Larson, OD. Squire, and JL. Humm. Reduction of respiratory motion artifacts in PET imaging of lung cancer by respiratory correlated dynamic PET: Methodology and comparison with respiratory gated PET. *J. Nucl. Med.*, 44(10):1644–1648, 2003.

[36] AJ. Reader, S. Ally, F. Bakatselos, R. Manavaki, RJ. Walledge, AP. Jeavons, PJ. Julyan, S. Zhao, DL. Hastings, and J. Zweit. One-pass list-mode EM algorithm for high resolution 3D PET image reconstruction into large arrays. *IEEE T. Nucl. Sci*, 49:693–699, 2002.

[37] David Rey. *Détection et quantification de processus évolutifs dans des images médicales tridimensionnelles : application à la sclérose en plaques.* Thèse de sciences, Université de Nice Sophia-Antipolis, October 2002.

[38] OG. Rousset, Y. Ma, and AC. Evans. Correction for partial volume effects in PET: Principle and validation. *J. Nucl. Med.*, 39(5):904–11, 4 1998.

[39] D. Rueckert, L.I. Sonoda, C. Hayes, D.L.G. Hill, M.O. Leach, and D.J. Hawkes. Non-rigid registration using free-form deformations: Application to breast MR images. *IEEE Transactions on Medical Imaging*, 18(8):712–721, 1999.

[40] J.A. Schnabel, D. Rueckert, M. Quist, J.M Blackall, A.D Castellano-Smith, T. Hartkens, G.P Penney, W.A. Hall, H. Liu, C.L. Truwit, F.A.Gerritsen, D.Hill, and D. Hawkes. A generic framework for non-rigid registration based on non-uniform multi-level free-form deformations. In W.J. Niessen and M. A. Viergever, editors, *Medical Image Computing and Computed-Assisted Intervention - MICCAI*, pages 573–581, 2001.

[41] W.P. Segars. *Development of a new dynamic NURBS-based cardiac-torso (NCAT) phantom.* PhD thesis, The University of North Carolina, 2001.

[42] Y. Seppenwoolde, H. Shirato, K. Kitamura, S. Shimizu, M. van Herk M, JV. Lebesque JV, and K. Miyasaka. Precise and real-time measurement of 3D tumor motion in lung due to breathing and heartbeat, measured during radiotherapy. *Int J Radiat Oncol Biol Phys.*, 53(4):822–34, July 2002.

[43] L. Shepp and Y. Vardi. Maximum likelihood reconstruction for emission tomography. *IEEE Trans. Med. Imag.*, 1(2):113–122, 1982.

[44] H.A. Shih, S.B. Jiang, K.M. Aljarrah, K.P. Dopke, and N.C. Choi. Planning target volume determined with fused CT images of fast, breath-hold, and four second simulation CT scans to account for respiratory movement in 3D-CRT in lung cancer. In *Annual meeting of The American Society for Therapeutic Radiology and Oncology*, New orleans, LA, October 5-8 2002.

[45] S. Shimizu, H. Shirato, K. Kagei, T. Nishioka, X. Bo, H. Dosaka-Akita, S. Hashimoto, H. Aoyama, K. Tsuchiya, and K. Miyasaka. Impact of respiratory movement on the computed tomographic images of small lung tumors in three-dimensional (3D) radiotherapy. *Int J Radiat Oncol Biol Phys.*, 46(5):1127–33, Mar 2000.

[46] J. Skalski, R.L Wahl, and CR. Meyer. Comparison of mutual information-based warping accuracy for fusing body CT and PET by 2 methods: CT mapped onto PET emission scan versus CT mapped onto PET transmission scan. *J. Nucl.Med.*, 43(9):1184–7, Sep 2002.

[47] P. Slomka, D. Key, C. Przetak, and R.P. Baum. Automated nonlinear 3D registration of 18ffdg wholebody pet with thoracic CT. In *2001 SNM Annual Meeting Toronto*, June 2001.

[48] Y.C. Tai, K.P. Lin, C.K. Ho, S.C.H Huang, and E.J. Hoffman. Utilization of 3D elastic transformation in the registration of chest X-ray CT and whole-body PET. *IEEE Trans. Nuclear Science*, 44:1606–1612, 1997.

[49] Division of Nuclear Medicine University of Washington. SimSET homepage. url.

[50] J.J. Bourdin V. Boyer. A faster algorithm for 3D discrete lines. *Eurographics*, 1998.

[51] JN Yu, FH Fahey, BA Harkness, HD Gage, CG Eades, and JW Keyes Jr. Evaluation of emission-transmission registration in thoracic PET. *J. Nucl. Med.*, 34(11):1777–1780, Nov. 1994.

Unité de recherche INRIA Sophia Antipolis
2004, route des Lucioles - BP 93 - 06902 Sophia Antipolis Cedex (France)

Unité de recherche INRIA Futurs : Parc Club Orsay Université - ZAC des Vignes
4, rue Jacques Monod - 91893 ORSAY Cedex (France)
Unité de recherche INRIA Lorraine : LORIA, Technopôle de Nancy-Brabois - Campus scientifique
615, rue du Jardin Botanique - BP 101 - 54602 Villers-lès-Nancy Cedex (France)
Unité de recherche INRIA Rennes : IRISA, Campus universitaire de Beaulieu - 35042 Rennes Cedex (France)
Unité de recherche INRIA Rhône-Alpes : 655, avenue de l'Europe - 38334 Montbonnot Saint-Ismier (France)
Unité de recherche INRIA Rocquencourt : Domaine de Voluceau - Rocquencourt - BP 105 - 78153 Le Chesnay Cedex (France)

Éditeur
INRIA - Domaine de Voluceau - Rocquencourt, BP 105 - 78153 Le Chesnay Cedex (France)
http://www.inria.fr
ISSN 0249-6399